Journal of Alloys and Compounds 509 (2011) 4352–4356

Contents lists available at ScienceDirect

Journal of Alloys and Compounds

journal homepage: www.elsevier.com/locate/jallcom

Microstructure of Ti–V–Mn BCC alloys before and after hydrogen absorption–desorption

Junko Matsuda*, Yumiko Nakamura, Etsuo Akiba

Energy Technology Research Institute (ETRI), National Institute of Advanced Industrial Science and Technology (AIST), 1-1-1 Higashi, Tsukuba, Ibaraki 305-8565, Japan

ARTICLE INFO

Article history:
Received 11 November 2010
Received in revised form 7 January 2011
Accepted 8 January 2011
Available online 14 January 2011

Keywords:
Ti–V–Mn alloy
Body-centered cubic alloy
Hydrogenation
Twin boundary
Transmission electron microscopy

ABSTRACT

Microstructure of Ti–V–Mn BCC alloys before and after hydrogen absorption–desorption was investigated using transmission electron microscopy. Strain contrast with spacing of 5–50 nm was observed along (1 0 1) planes of the BCC phase in both the as-cast alloys and the alloys after hydrogenation–dehydrogenation. Twin boundaries and stacking faults with spacing of 5–100 nm were introduced into the Ti–V–Mn BCC alloys after hydrogen absorption–desorption. These were parallel to the (1 0 1) of BCC alloys and (1 $\bar{1}$ 1) of remained FCC hydrides. The twin boundaries and stacking faults were formed due to accommodation of the shear stress during hydrogenation accompanied by large anisotropic expansion along the *c*-axis direction in the Ti–V–Mn BCC alloys.

1. Introduction

Ti-based BCC alloy is one of the most promising candidates for hydrogen storage alloys for onboard storage of hydrogen because of the highest capacity among interstitial hydrides, easiness of activation and so on. Therefore, Ti-based alloys have been intensively investigated since they were reported by one of the authors [1–4]. Ti-based BCC alloys are solid solution of constituent elements such as Ti, V, Cr, Mn and Mo, while most of other interstitial hydrides are intermetallic compounds. The mechanical properties of solid solution and intermetallic compound are significantly different. The former is ductile and the latter is brittle. Such mechanical properties have a great effect on the microstructure evolution and introduction of lattice defects in hydrogen absorbing alloys, which expand and contract 20–30% in volume with hydrogenation and dehydrogenation at around room temperature. From the application point of view, microstructure is closely related to reaction kinetics and degradation of hydrogen capacity. Understanding of microstructure change and introduction of defects with hydrogenation are critical to improve the hydrogenation properties mentioned above.

As for Ti–V–Mn BCC alloys, it was suggested that the distribution of Ti and V with a period of 20 nm or less was formed by the spinodal decomposition during solidification of Ti–V–Mn melting [5]. However, details of these structures have not been reported yet as far as the authors know, while for the conventional intermetallic hydrogen storage alloys, change in microstructures and defects introduced into the lattice during hydrogenation–dehydrogenation have been studied [6,7].

In this work, microstructure of Ti–V–Mn BCC alloys before and after hydrogen absorption–desorption has been observed by transmission electron microscopy (TEM), in order to investigate the introduction of lattice defects during hydrogenation/dehydrogenation. Ti–V–Mn alloys with various compositions were investigated by TEM, since hydrogen absorbing/desorbing properties depend on respective contents and compositions of the BCC and C14 impurity phases in the Ti–V–Mn alloys.

2. Experimental procedure

Ti, V and Mn metals with higher than 99.9% purity were weighed out in molar ratios of $Ti_{3-x-y}V_xMn_{y+0.05}$ for 'the nominal composition' of $Ti_{3-x-y}V_xMn_y$. The $Ti_{3-x-y}V_xMn_y$ ($0.8 \le x \le 1.4$, $0.8 \le y \le 1.1$) samples were prepared using arc-melting on a water-cooled copper crucible under argon atmosphere. As-cast alloys with button shaped were crushed to 1–2 mm particles, and contained phases were identified by X-ray powder diffraction (XRD). Pressure–composition (*P–C*) isotherms were measured by the Sieverts method at 298 K under 5 MPa after evacuating at 423 K. The average chemical composition of the as-cast alloys was analyzed using scanning electron microscopy (SEM) and energy dispersive X-ray spectroscopy (EDS). Microstructure and the local distribution of constituent elements in those Ti–V–Mn alloys before and after hydrogen absorption–desorption were investigated using TEM. Samples for the TEM observation were prepared as follows: filling into brass tubes the alloy particles with epoxy resin, grinding them mechanically, and finally ion-milling with the cold stage cooled using liquid nitrogen. TEM used in this study were H-9000NAR by Hitachi High-Technologies Co. and JEM-2100F by JEOL Ltd.

* Corresponding author. Tel.: +81 29 861 4484; fax: +81 29 861 4711.
E-mail address: junko.matsuda@aist.go.jp (J. Matsuda).

0925-8388/$ – see front matter © 2011 Elsevier B.V. All rights reserved.
doi:10.1016/j.jallcom.2011.01.071

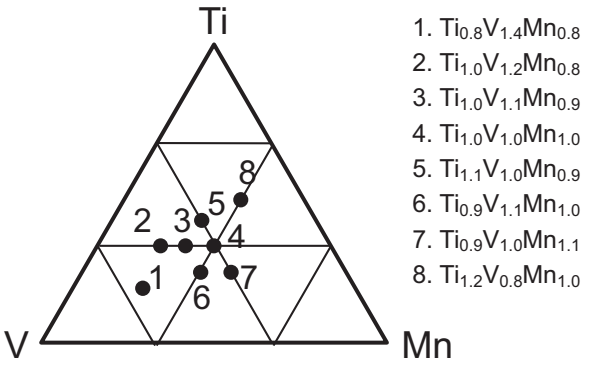

Fig. 1. Nominal composition of $Ti_{3-x-y}V_xMn_y$ alloys prepared in this study.

3. Results and discussion

3.1. Microstructure of Ti–V–Mn BCC alloys before hydrogen absorption–desorption

Fig. 1 shows the nominal composition of $Ti_{3-x-y}V_xMn_y$ alloys prepared in this study. The content of the BCC phase in each sample depended on the V content, which agrees with previous reports [8–10]. XRD patterns revealed that as-cast Sample 1 and Sample 2 with the V-rich composition contained the only BCC phase. In contrast, Sample 8 with the V-poor composition contained the C14 Laves phase more than 90 mass%. In the alloys with the same content of the V element, the fraction of the C14 phase increased with decreasing of Ti/Mn molar ratio: Sample 3 and Sample 4 contained 10 mass% or less of the C14 phase, however, 30–50 mass% in Sample 6 and Sample 7 were the C14 phase. Sample 5 with the Ti-rich composition had not only the C14 phase but also a Ti-based compound, which was detected by TEM–EDS. Ti oxide with a $ZrTiO_3$-type structure was reported to be an impurity in the Ti–V–Mn BCC alloys [2]. The content of the C14 phase was calculated using the "nominal composition" and local compositions of the BCC and C14 phases from the quantification results of TEM–EDS analysis. The average chemical composition of the as-cast samples was confirmed to correspond to the nominal composition by TEM–EDS while irradiating the wide range of the samples by electron beam as well as SEM–EDS.

Fig. 2 shows *P–C* isotherms of the first cycle for Samples 1, 3 and 6 measured at 298 K under 5 MPa of hydrogen. Lattice parameters of the BCC phase in Sample 1 and Sample 3 were 3.026–3.028 Å from XRD results, although the former was the BCC single phase and

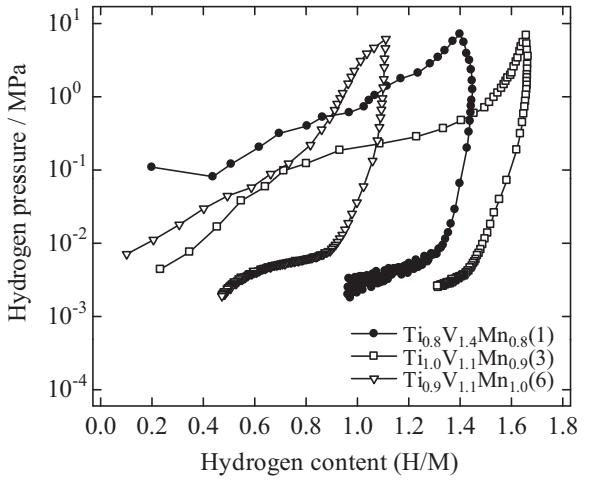

Fig. 2. *P–C* isotherms of the first cycle for Samples 1, 3 and 6 measured at 298 K under 5 MPa of hydrogen.

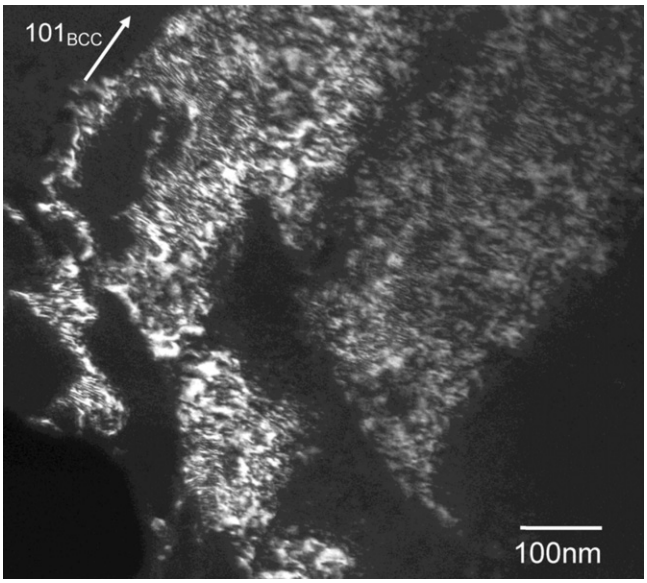

Fig. 3. Typical dark-field TEM image using a $1\,0\,1_{BCC}$ reflection of as-cast Sample 3 before hydrogenation. It is noted that strain contrast is visible with spacing of less than 50 nm.

the latter contained several mass percent of the C14 phase. The hydrogen capacity should not be discussed on the *P–C* isotherms measured under 5 MPa. However, hydrogen absorption pressures tended to increase with increasing of the V content in the as-cast alloys; Sample 1 with the V-rich composition exhibited a higher hydrogen absorbing pressure than Sample 3. Sample 6 exhibited smaller hydrogen content, since it contained more than 30 mass% of the C14 phase and the BCC phase with the average lattice parameter of 3.010 Å. In Sample 6, the V-rich BCC phase was detected in the vicinity of the interface between the BCC and C14 phases. In this sample containing a large quantity of the C14 phase, hydrogen absorption and desorption pressures seemed to be affected by local distributions of metal elements.

Fig. 3 shows a typical dark-field image of as-cast Sample 3 before hydrogenation using a $1\,0\,1_{BCC}$ reflection in the electron diffraction pattern. As shown in this image, strain contrasts with spacing of 5–50 nm were observed in the BCC particles for all the samples along the $(1\,0\,1)_{BCC}$. Spacing of the strain contrast along the $(1\,0\,1)_{BCC}$ plane tended to be narrow in the V-rich sample (Samples 1 and 2). It was considered that this contrast was related to the spinodal decomposition texture formed during the solidification of the Ti–V–Mn melting, which was reported by Iba and Akiba [3]. They suggested that the lattice strain was generated in the vicinity of the coherent interface between BCC phases which had a little difference in lattice parameters.

3.2. Microstructure of Ti–V–Mn BCC alloys after hydrogen absorption–desorption

Microstructure of Ti–V–Mn BCC alloys after one and/or five cycles of hydrogen absorption–desorption was investigated by TEM: *P–C* measurements at 298 K were repeated after heating the samples at 423 K for 3–5 h with evacuating by rotary pump. The strain contrasts with spacing of 5–50 nm were also observed in the Ti–V–Mn alloys after hydrogen absorption–desorption cycles. Fig. 4(a) and (b) shows high-resolution (HR) TEM images of Sample 1 ($Ti_{0.8}V_{1.4}Mn_{0.8}$) and Sample 7 ($Ti_{0.9}V_{1.0}Mn_{1.1}$) after five cycles of hydrogen absorption–desorption, which were taken from the direction of $[1\,1\,1]_{BCC}$ and $[1\,0\,0]_{BCC}$, respectively. Sample 1 was the BCC single phase. However, Sample 7 contained more than

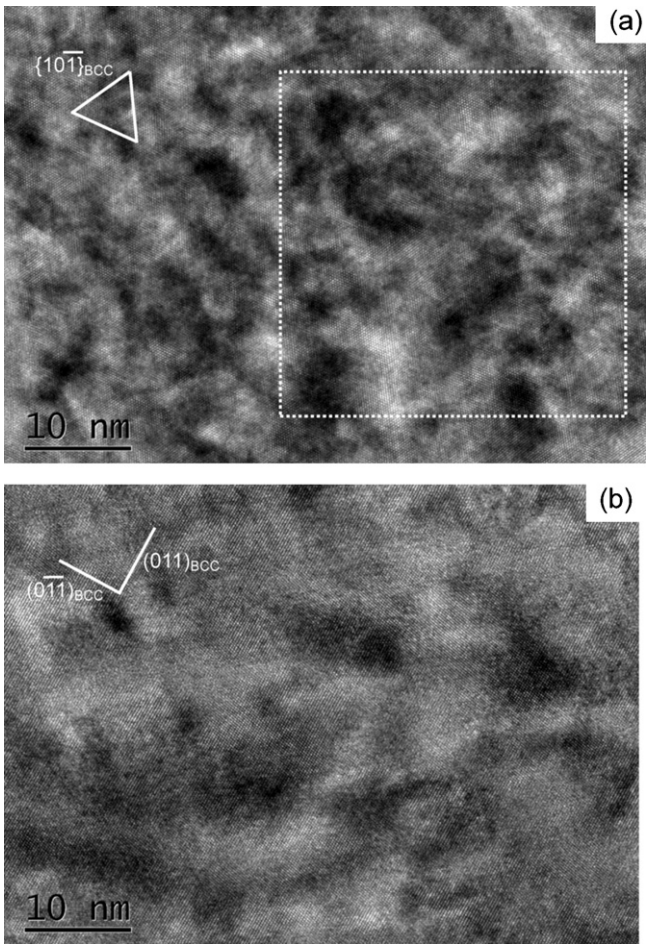

Fig. 4. High-resolution (HR) TEM images of (a) Sample 1 and (b) Sample 7 after five cycles of hydrogen absorption–desorption, which were taken from the direction of $[1\,1\,1]_{BCC}$ and $[1\,0\,0]_{BCC}$, respectively. In the BCC phase with the V-rich composition, fine strain contrast was observed almost all over the particles.

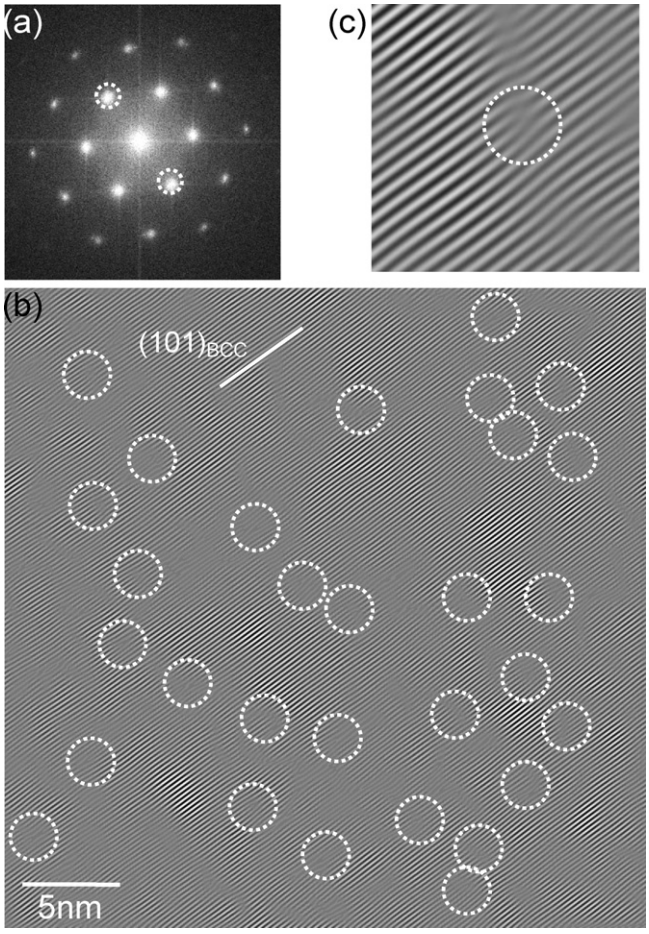

Fig. 5. (a) Fourier function transformation (FFT) image from the HRTEM image in Fig. 4(a) and (b) inversed FFT image from filtered FFT of Fig. 5(a) and (c) an enlarged image at a part of Fig. 5(b). The strain contrast corresponded to the lattice defects including the edge dislocation with the Burgers vector perpendicular to $(1\,0\,1)_{BCC}$ planes, as indicated by dotted circles in Fig. 5(b).

50 wt% of the C14 phase, and the composition of the BCC in the matrix was $Ti_{0.92}V_{1.06}Mn_{1.02}$. As shown in Fig. 4(a), fine strain contrast with spacing smaller than 10 nm tended to be observed all over the V-rich BCC phase, regardless before and after hydrogen absorption–desorption. On the other hand, there was also the strain contrast with spacing larger than 20 nm in the samples except Sample 1 and Sample 2 with the V-rich composition.

Fig. 5(a) shows Fourier function transformation (FFT) image from the dotted rectangular area in Fig. 4(a), and Fig. 5(b) the inversed FFT image from the filtered FFT in Fig. 5(a). Edge-like dislocations are indicated by dotted circles in Fig. 5(b), and the enlarged image is shown in Fig. 5(c). As shown in these figures, the strain contrasts corresponded to the lattice defects including the edge dislocation with the Burgers vector perpendicular to $(1\,0\,1)_{BCC}$ planes.

Lattice defects introduced into the Ti–V–Mn BCC alloys during hydrogen absorption–desorption were twin boundaries and stacking faults along $(1\,0\,1)$ planes of the BCC alloys and $(1\,\bar{1}\,1)$ of the remained FCC hydrides. Fig. 6 shows the low-magnification TEM image and the selected-area electron diffraction pattern (SAEDP) of Sample 2 ($Ti_{1.0}V_{1.2}Mn_{0.8}$) after five cycles of hydrogen absorption–desorption. This particle was found to be the remained FCC hydride with the lattice parameter of about 0.4 nm from the SAEDP. Circled spots in the SAEDP were formed by mirror operation against $(1\,\bar{1}\,1)$ plane. These results revealed that twin boundaries were formed parallel to the $(1\,\bar{1}\,1)$ planes of FCC crystals with spacing of 20–100 nm in Sample 2 after hydrogen absorption–desorption.

Fig. 7 shows the HRTEM image of Sample 6 ($Ti_{0.9}V_{1.1}Mn_{1.0}$) after five cycles of hydrogen absorption–desorption. Significant stacking faults along the $(1\,\bar{1}\,1)_{FCC}$ were also formed as well as twin boundaries after hydrogen absorption–desorption. These twin boundaries and stacking faults were observed along $(1\,0\,1)$ planes in the BCC phase, and were formed due to shear stress during hydrogena-

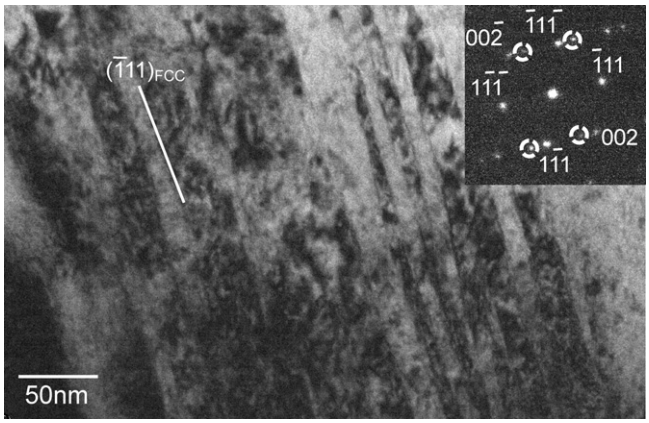

Fig. 6. TEM image and selected area electron diffraction pattern (SAEDP) of the remained FCC hydride in Sample 2 after five cycles of hydrogen absorption–desorption, which was taken from the direction of $[1\,1\,0]_{FCC}$.

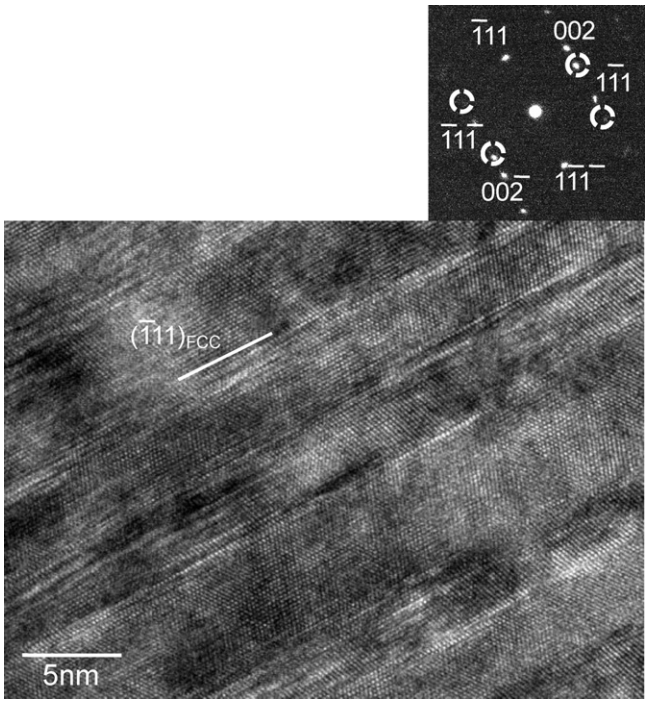

Fig. 7. Typical HRTEM image of the remained FCC hydride particle in Sample 6 after five cycles of hydrogen absorption–desorption, which was obtained at the incident of $[1\,1\,0]_{FCC}$.

tion accompanied by phase transformation from BCC to FCC: the significant anisotropic expansion along *c*-axis direction occurred at the same time [11]. The twin boundaries and stacking faults were introduced with spacing of 5–100 nm in the BCC or FCC particles for all the samples studied after five cycles of hydrogen absorption–desorption except Ti-rich Sample 5, in which stacking faults were only observed. In addition, it was confirmed that twin boundaries were already introduced after the first cycle of hydrogen absorption–desorption regarding several samples. It was also reported that the twin boundaries were formed during the hydrogenation of V pure metal [12,13]. On the other hand, lattice defects in the C14 phase were not observed in the present work.

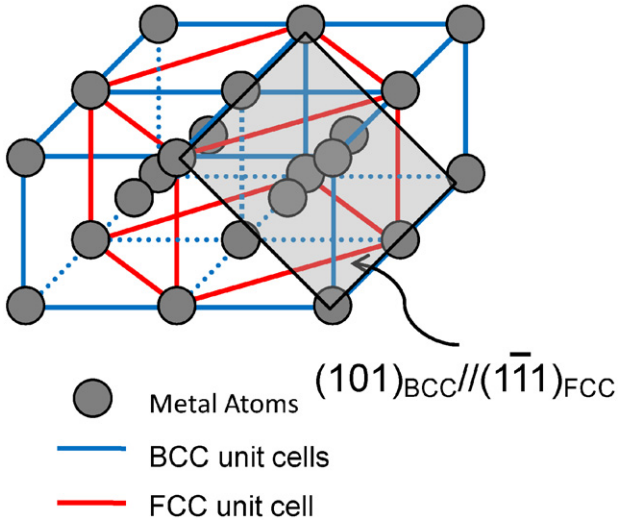

Fig. 8. Orientation relationship between BCC alloy and FCC hydride, assuming that the arrangement of metal atoms does not change during hydrogenation although anisotropic expansion occurs.

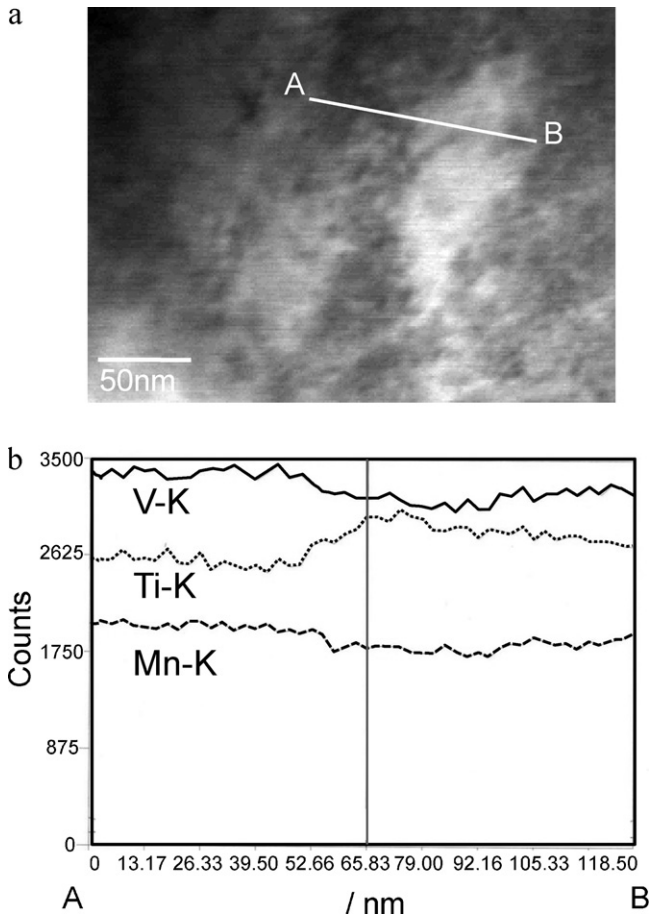

Fig. 9. TEM–EDS analysis on Sample 3 after the first *P–C* measurement: (a) a scanning TEM image; (b) distribution of Ti, V and Mn along the line AB in the image (Fig. 9(a)). As shown in this figure, the V content increased in the region with black contrast, and decreased in the region with white contrast. The former corresponded to the region which contains a larger amount of lattice strain than the latter.

As shown in Fig. 8, the direction of $[1\,0\,0]$ in the BCC crystal corresponds to the direction of $[1\,\bar{1}\,0]$ in the FCC, assuming that the arrangement of metals does not changed during hydrogenation even though anisotropic volume expansion. Although it is difficult to reconcile the orientation relationship with $(1\,0\,1)_{BCC}$ twin related hydride precipitates, the BCC lattice transforms homogeneously to the FCC structure with forming of $(1\,0\,1)$ twins as a self-accommodation effect.

3.3. Relationship between strain contrast and chemical composition

Any significant difference in the distribution of metal elements with periodicity of less than 20 nm was not detected from the TEM–EDS results in this study. However, the amounts of lattice strain were related to the V content in Ti–V–Mn BCC alloys. Fig. 9(a) and (b) shows the result of TEM–EDS mapping for Sample 3 ($Ti_{1.0}V_{1.1}Mn_{0.9}$) after the first *P–C* measurement. Fig. 9(b) shows the distribution of Ti, V and Mn along the line AB in a scanning TEM image of Fig. 9(a). As shown in these figures, the V content increased in the region with black contrast, and decreased in the white region. The former corresponds to the region which contains a larger amount of lattice strain than the latter. This agrees with the result that the strain contrast with spacing of less than 10 nm was visible all over the particles in the V-rich Sample 1 and Sample 2, as shown in Figs. 4(a) and 5. The effects of the lattice strain in the Ti–V–Mn BCC alloys is not clear on the hydrogen

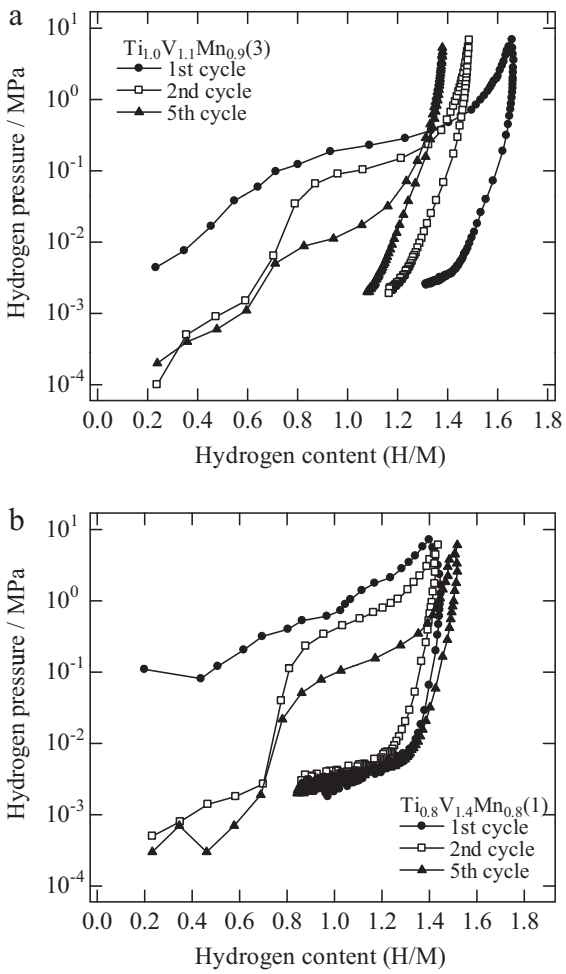

Fig. 10. *P–C* isotherms of the first, second and fifth cycles for (a) Sample 3 and (b) Sample 1, measured at 298 K under 5 MPa of hydrogen.

absorbing and desorbing properties, however, it is possible that the lattice strain improves hydrogen desorbing property of the Ti–V–Mn alloys. Fig. 10 shows *P–C* isotherms of the first, second and fifth cycles for (a) Sample 3 and (b) Sample 1, measured at 298 K under 5 MPa of hydrogen. Hydrogen contents of Sample 3 and Sample 1 are H/M = 1.6 and H/M = 1.4, respectively, in the first cycle of hydrogen absorption–desorption under this condition. The hydrogen content in the fifth cycle of Sample 3 decreased to about 1.4, while that of Sample 1 did not decrease. It was found that hydrogen desorbing capacity does not degrade in the V-rich Ti–V–Mn alloys containing the considerable amount of nano-size lattice strain. The V-rich BCC phase was reported to segregate in the vicinity of the interface between the BCC and C14 phases [5,9]. Investigation of the effects of the interface between the BCC and C14 phases on the hydrogen absorption–desorption properties such as hydrogen capacity and desorbing equilibrium pressures is in progress.

4. Conclusions

Ti–V–Mn BCC alloys before and after hydrogenation–dehydrogenation have been investigated using transmission electron microscopy. Summary of results are as follows:

(1) The strain contrasts with spacing of 5–50 nm were observed in the as-cast Ti–V–Mn BCC alloys, which corresponded to the lattice defects including edge dislocation components along $(1\,0\,1)_{BCC}$ planes. These strain contrasts were also observed in the BCC alloys after hydrogen absorption–desorption, while spacing of the strain contrast tended to increase in the V-rich BCC region.
(2) After hydrogen absorption–desorption, twin boundaries and stacking faults along the (1 0 1) planes of the BCC alloy and the $(1\bar{1}1)$ of the remained FCC hydride were observed. These were formed by self-accommodation due to shear stress during hydrogenation accompanied by the significant anisotropic expansion of the *c*-axis direction.

It is important to understand the microstructure evolution during the hydrogenation reaction, in order to improve the hydrogen effective capacity and desorbing equilibrium pressures at ambient condition by controlling their microstructures.

Acknowledgments

This work was supported by The New Energy and Industrial Technology Development Organization (NEDO) under Advanced Research on Hydrogen Storage Materials (HYDRO-STAR).

References

[1] J. Huot, E. Akiba, H. Iba, J. Alloys Compd. 228 (1995) 181–187.
[2] J. Huot, E. Akiba, Y. Ishido, J. Alloys Compd. 231 (1995) 85–89.
[3] H. Iba, E. Akiba, J. Alloys Compd. 231 (1995) 508–512.
[4] M. Okada, T. Kuriiwa, T. Tamura, H. Takamura, A. Kamegawa, J. Alloys Compd. 330–332 (2002) 511–516.
[5] H. Iba, E. Akiba, J. Alloys Compd. 253–254 (1997) 21–24.
[6] H. Inui, T. Yamamoto, M. Hirota, M. Yamaguchi, J. Alloys Compd. 330–332 (2002) 117–124.
[7] B. Decamps, J.–M. Joubert, R. Cerny, A. Percheron-Guegan, J. Alloys Compd. 404–406 (2005) 570–575.
[8] T. Gamo, Y. Moriwaki, N. Yanagihara, T. Iwaki, J. Less-Common Met. 89 (1983) 495–504.
[9] E. Akiba, H. Iba, Intermetallics 6 (1998) 461–470.
[10] M. Shibuya, J. Nakamura, H. Enoki, E. Akiba, J. Alloys Compd. 475 (2009) 543–545.
[11] Y. Nakamura, E. Akiba, J. Alloys Compd. 311 (2000) 317–321.
[12] S. Takano, T. Suzuki, Acta Metall. 22 (1974) 265–274.
[13] M.P. Cassidy, B.C. Muddle, T.E. Scott, C.M. Wayman, J.S. Bowles, Acta Metall. 25 (1979) 829–838.